Selective Oxidation of Benzyl Alcohol with Oxygen Catalyzed by Vanadia Supported on Nitrogen-Containing Ordered Mesoporous Carbon Materials

Xin-Tong Yi[1] · Tian-Lu Wang[1] · Lin-Zhi Wen[1] · Jie Xu[1] · Bing Xue[1]

Abstract

Liquid-phase selective oxidation of alcohols to aldehydes using molecular oxygen as an oxidant is one of the most important transformations in organic synthesis and green chemistry. In this work, nitrogen-containing ordered mesoporous materials (NOMCs) were prepared and utilized as supports to load vanadia. The physical and chemical properties of the synthesized V_xO_y/NOMC materials were characterized by N_2 adsorption–desorption, XRD, TEM, Raman, and XPS. The characterization results exhibited that NOMC could well disperse vanadia species and there was a steady interaction between V and N of NOMC. In selective oxidation of benzyl alcohol using oxygen as an oxidant, the synthesized V_xO_y/NOMC materials showed good and stable catalytic performance, affording a maximum yield of benzaldehyde up to 80% at 95 °C.

Graphic abstract
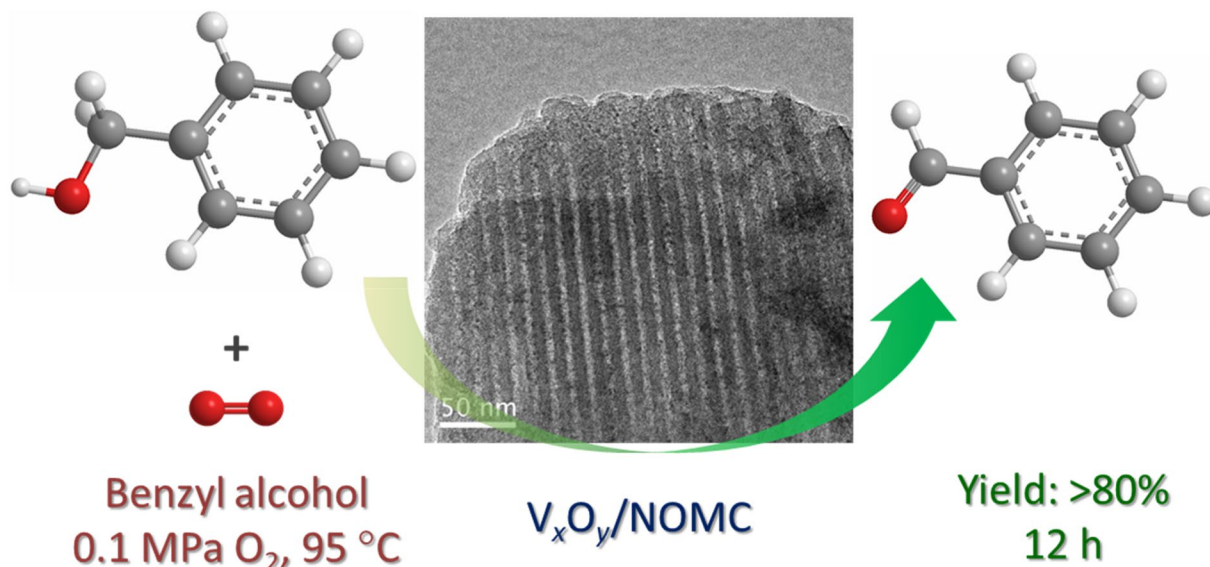
Keywords Graphitic carbon nitride (g-C_3N_4) · Vanadium oxide · Benzyl alcohol · Benzaldehyde · Selective oxidation

✉ Jie Xu
shine6832@163.com

✉ Bing Xue
xuebing_cn@163.com

Extended author information available on the last page of the article

1 Introduction

As the simplest aromatic aldehyde, benzaldehyde is extensively used in the synthesis of pharmaceuticals, perfumes, dyestuff, pesticides, and a wide range of chemical

intermediates [1, 2]. Industrially, benzaldehyde is mainly manufactured by liquid-phase hydrolysis of benzyl chloride and by the stoichiometric oxidation of toluene [3–5]. However, the two conventional processes suffer from chlorine contamination and substantial metal-containing pollutants [6, 7], respectively. Alternatively, selective oxidation promoted by heterogeneous catalysts offers a more sustainable route for the synthesis of benzaldehyde owing to the easy recovery and reusability of catalysts [8–10]. Among various oxidants including H_2O_2, N_2O, and O_2, O_2 is inexpensive and widely available, and therefore selective oxidation of benzyl alcohol with O_2 has been regarded as a more environmentally clean process in the viewpoint of green chemistry [11–13]. However, because the target molecule (i.e. benzaldehyde) is more chemically active than benzyl alcohol under the oxidative circumstance, it is of interest to develop an efficient heterogeneous catalyst that could afford high selectivity under mild reaction conditions [14–16].

A variety of heterogeneous catalyst systems have been developed for the selective oxidation of benzyl alcohol [17, 18]. Wherein, supported precious metals including Au [19–21], Pd [8, 16, 22, 23], Pt [24–27], have been widely recognized as the most efficient catalysts. However, such noble catalysts are expensive and rare. Moreover, in order to achieve high selectivities, most of them need to be operated in a strongly basic medium [22, 28]. In this sense, there remains a challenge to explore a new, low-cost, and high-performance base-metal-based catalyst for the selective oxidation process. Vanadium oxide is a classical catalyst widely applied in numerous oxidation reactions, as it possesses highly feasible reactivity and remarkable stability [29]. It has been also reported that vanadia can efficiently promote the selective oxidation of alcohols [30–34]. Nevertheless, harsh conditions, such as high temperatures and long reaction time, were always required to reach a high productivity. On the other hand, it is well recognized that in many oxidative reactions [35, 36], the catalytic activity and selectivity to the desired aldehyde are mainly dependent on the dispersion of vanadia [5]. Specifically, dispersed vanadia sites are the key centers for both catalytic activity and selectivity.

Recently, nitrogen-containing ordered mesoporous carbon (NOMC) materials have attracted growing interest in various research fields [37]. The incorporation of nitrogen into the carbon frameworks has expanded the upgrading application of NOMC materials in electrochemistry [38, 39], supercapacitor [40, 41], gas storage [42, 43], heterogeneous catalysis [44–46], etc. In the aspect of heterogeneous, NOMC materials possess multiple types of nitrogen-containing chemical functionalities such as pyridinic, pyrrolic, and graphitic nitrogen species [47]. Wang et al. found that NOMC materials featuring various nitrogen species and mesostructures could promote selective oxidation/dehydrogenation of ethylbenzene [44, 48]. Recently, Watanabe et al.

revealed that nitrogen-doped activated carbons were able to catalyze the oxidation of benzyl alcohol [49]. The catalytic reaction was performed under high temperature (120 °C) and the final conversion of alcohol was less than 25%. That is, if nitrogen-containing carbon material is used as a sole catalyst, the catalytic activity in the oxidative reaction is indeed dissatisfactory.

On the other hand, the nitrogen-containing species of NOMC offer its potential anchoring sites to load metal and/or metal oxide [37, 50]. Inspired by the characteristic of NOMC, in this work, we utilized NOMC as support to load vanadia. NOMC could well disperse vanadia on its surface through a stable interaction between V and nitrogen of NOMC. In the ambient selective oxidation of benzyl alcohol, the synthesized V_xO_y/NOMC materials showed high catalytic performance.

2 Experimental Section

2.1 Catalyst Preparation

2.1.1 Preparation of NOMC

NOMC was synthesized using F127 (triblock copolymer) as a soft template by means of a one-pot templating method under an aqueous phase [44]. F127 (4 g) and of 1,3,5-trimethylbenzene (0.96 g) were added into 100 mL of H_2O, and then stirred vigorously until complete dissolution. m-aminophenol (MAP, 2.2 g), hexamethylenetetramine (1.4 g), and aqueous ammonia (2.6 mL) were added into the above solution. After 1 h of stirring, the mixture was heated at 80 °C for 24 h, and then filtrated. The obtained solid was rinsed with water and dried. Subsequently, the dried solid was calcinated to 600 °C with a heating rate of 1 °C min^{-1} under N_2 atmosphere and then heated for another 2 h. The final solid was designated as NOMC.

2.1.2 Preparation of V_xO_y/NOMC

NOMC was initially dried at 100 °C for 1 h, and then immersed into ethanol solution (40 mL) containing vanadyl (IV) acetylacetonate ([$VO(acac)_2$]). The suspension was stirred for 30 min and then heated at 60 °C under stirring until the removal of ethanol. After that, the solid was transferred into a quartz boat and placed in a tubular furnace, and then heated to the desired temperature with a heating ramp of 5 °C min^{-1} and tempered for another 2 h under the flow of nitrogen gas (10 mL min^{-1}). The obtained black powder was designated as wV_xO_y/NOMC-T, where w and T represented the loading amount (5−15%) of V, and the calcination temperature (350−500 °C). Unless specified, the calcination temperature was 400 °C.

2.2 Material Characterization

Nitrogen physical adsorption experiments were performed on an ASAP 2020 analyzer (Micromeritics). The specific surface area and pore size distributions of the analyzed samples were determined by the BET and BJH methods, respectively.

X-ray diffraction (XRD) patterns of the materials were tested on a D/max 2500 PC X-ray diffractometer (Rigaku) equipped with Cu-K_α radiation.

Raman spectra were collected on a Lab Ram HR evolution spectrometer (Jobin Yvon) using a 532 nm line as the excitation source.

Transmission electron microscopy (TEM) experiments were carried out on a 2010 electron microscope (JEOL).

X-ray photoelectron spectra (XPS) were analyzed on an ESCALAB 250XI spectrometer (Thermo) adopting an Mg/Al anode as an X-ray source.

The adsorption tests of benzyl alcohol and benzaldehyde were based on a method reported previously [51]. Benzyl alcohol or benzaldehyde (0.1, 0.3, and 0.5 mL) was dissolved in 5 mL of toluene. Next, 50 mg of dried materials were added into the solution, and the mixture was stirred at 35 °C for 0.5 h.

2.3 Catalytic Evaluation

Selective oxidation reactions of benzyl alcohol (BZA) were performed in a three-necked flask equipped with a condenser. BZA (1 mmol) and toluene (5 mL) were mixed firstly in a flask, followed by the addition of the catalyst (100 mg). The mixture was heated up to 95 °C, then flushed with oxygen (20 mL min^{-1}) under stirring. A small amount of the reaction mixture was collected periodically, centrifuged and the resultant liquid was analyzed by gas chromatography equipped with a capillary column (SE-54) and FID detector. The liquid phase of the reaction contained BZA, benzaldehyde, and a trace of acid. The carbon balance was nearly 100%, and the BZA conversion and selectivity to benzaldehyde were calculated based on an area-normalization method of GC, and the corresponding calculation equations are as follows:

$$Conv. = \frac{A_{BZL} \times f_{BZL} + A_{BA} \times f_{BA}}{A_{BZA} + A_{BZL} \times f_{BZL} + A_{BA} \times f_{BA}}, \quad Sel. = \frac{A_{BZL} \times f_{BZL}}{A_{BZL} \times f_{BZL} + A_{BA} \times f_{BA}},$$

$$Yield = Conv. \times Sel.$$

where A, and f are the peak areas of GC, and response factors for each product, respectively.

3 Results and Discussions

3.1 Material Structures

The porous properties of NOMC and its supporting materials were analyzed by N_2 adsorption–desorption. NOMC has a type-IV isothermal curve with a remarkable hysteresis loop in the range of $p/p_0 = 0.4$–0.6 (Fig. 1A), indicating the material possesses mesoporous structures with a narrow pore size distribution (Fig. 1B). The 5V$_x$O$_y$/NOMC

Fig. 1 N$_2$ adsorption–desorption isotherms (**A**) of NOMC and V$_x$O$_y$/NOMC materials and the corresponding pore size distributions (**B**)
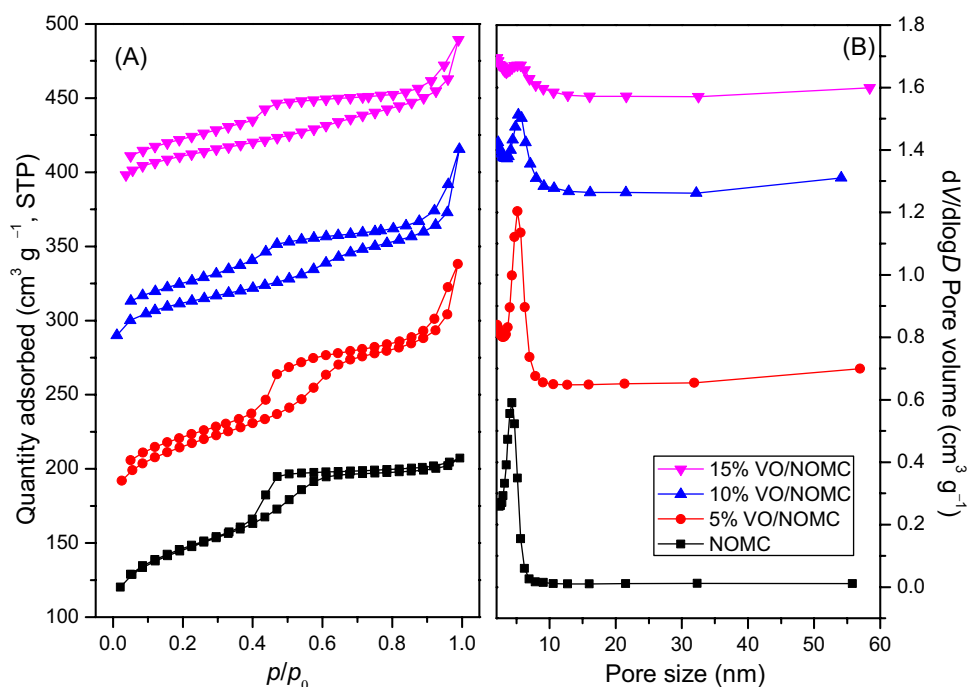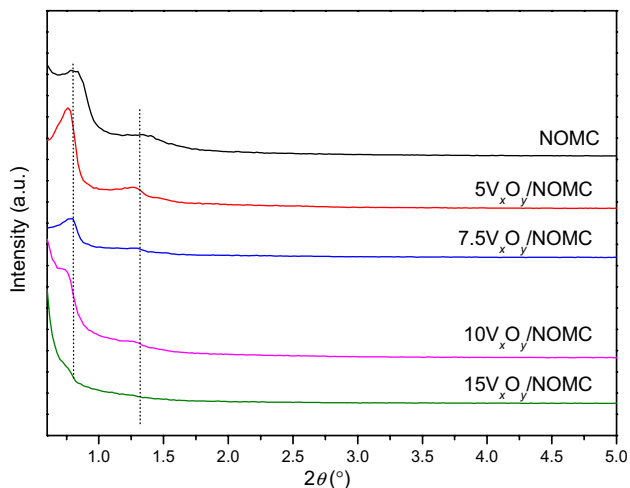
Table 1 Surface areas and porous properties of the materials

Sample	S_{BET} ($m^2\ g^{-1}$)	Pore size (nm)	Pore volume ($cm^3\ g^{-1}$)
NOMC	474	4.3	0.32
5V$_x$O$_y$/NOMC	385	5.1	0.37
10V$_x$O$_y$/NOMC	260	5.2	0.28
15V$_x$O$_y$/NOMC	213	5.6	0.22

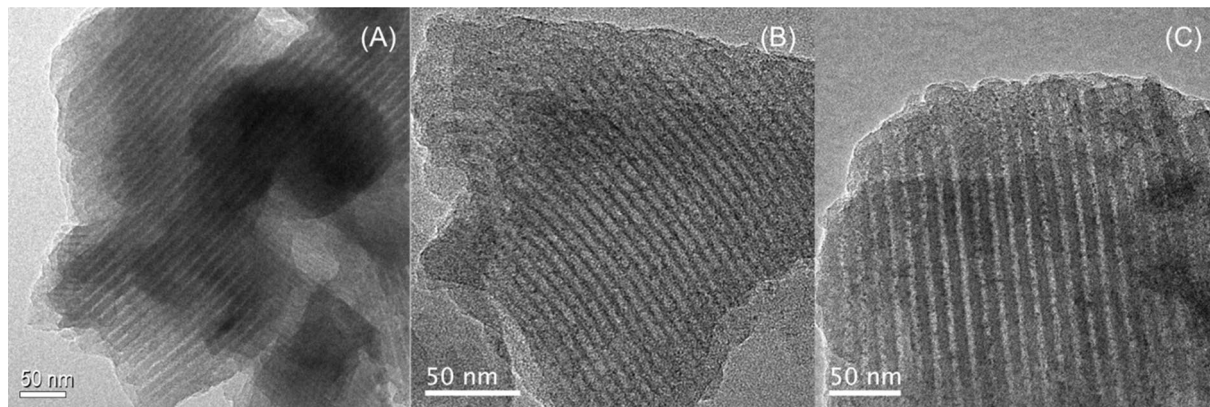**Fig. 2** Small-angle XRD patterns of NOMC and V$_x$O$_y$/NOMC materials

material also has typical mesopores like NOMC. Whereas as the loading amount of vanadia of V$_x$O$_y$/NOMC is further increased, the desorption branches of the isothermal curves in the low range of relative pressures are not reversible. The phenomenon is possibly due to the partial decomposition of the materials under very low pressure of analytic conditions, as found in previous work [46]. The surface area and pore volume (Table 1) of NOMC are 474 $m^2\ g^{-1}$ and

0.32 $cm^3\ g^{-1}$, respectively. With the increase of the loading amount of vanadia, the surface areas and pore volumes of V$_x$O$_y$/NOMC decrease gradually while the pore size shows a slight increase. The variation in surface area and porous properties suggests that vanadia has been supported on NOMC, while some porous structures of NOMC suffer partial collapse after the incorporation of vanadia.

The mesoporous structures of NOMC and its supported V$_x$O$_y$/NOMC materials were further investigated by small-angle XRD (Fig. 2). The XRD patterns of NOMC show two diffraction peaks at 2θ of 0.8 and 1.32°, corresponding to the (100) and (110) reflections of two-dimensional hexagonal symmetry [44, 52]. The two pronounced diffraction peaks further confirm the existence of ordered mesoporous structures in NOMC. Similar diffraction peaks have also been observed in the cases of V$_x$O$_y$/NOMC materials. However, compared with that obtained in the XRD pattern of the pristine NOMC, the positions of the diffraction peaks of V$_x$O$_y$/NOMC are shifted towards lower 2θ values, suggesting that V$_x$O$_y$/NOMC materials have much larger lattice parameters than NOMC. Furthermore, in the case of 15V$_x$O$_y$/NOMC, the intensity of the diffraction peak becomes much weaker and the (110) reflection disappears. This means that vanadia with excessive loading amount would destroy the ordered mesoporous structures of NOMC, which is responsible for the decline of surface area and pore volume from NOMC to 15V$_x$O$_y$/NOMC (Table 1).

TEM was used to observe the micromorphology of the materials and the TEM images of NOMC and V$_x$O$_y$/NOMC materials are displayed in Fig. 3. The image of NOMC shows ordered shutter-like strips, further verifying the ordered mesoporous structures of the material. The images of V$_x$O$_y$/NOMC materials also demonstrate regular mesoporous channels like NOMC. Between these channels, there exist abundant small particles, which are attributed to vanadia species. Directly judging from the TEM images of V$_x$O$_y$/NOMC, the particle sizes are ca. 3 nm, suggesting that

Fig. 3 TEM images of NOMC (**A**), 5V$_x$O$_y$/NOMC (**B**), and 10V$_x$O$_y$/NOMC (**C**)

vanadia nanoparticles are well dispersed in the mesoporous channels of NOMC support.

Figure 4 depicts the wide-angle XRD patterns of the materials. All the patterns reveal intensive diffraction peaks at 2θ degrees of ca. 22.3° as well as broad shoulders at ca. 43°. The appearance of two peaks is contributed to the (002) and (100) reflections of disordered graphite [42, 53], respectively. In the comparison that of the pure NOMC, the peak intensity of V$_x$O$_y$/NOMC becomes much lower, especially as the loading amount of the vanadia is increased. This means that the crystallinity of the graphitic framework of NOMC is partially damaged upon the loading of vanadia, possibly due to the interaction between vanadia and nitrogen species in the graphitic matrix of NOMC (discussed below).

The graphitic structures of NOMC and V$_x$O$_y$/NOMC have also been confirmed by Raman spectroscopy (Fig. 5). The Raman spectra of the materials display two distinct peaks centered at 1344 and 1591 cm^{-1}, which are indexed as D (sp3-hybridized carbon atoms in defects) and G (sp2-hybridized carbon atoms in graphitic lattice) bands, respectively. The intensity of the G band is apparently higher than the D band in the spectrum of NOMC, namely the material possesses a high I_G/I_D ratio. However, the relative ratios are weakened in the cases of V$_x$O$_y$/NOMC materials. The change points out that the percentage of the original sp2-hybridized carbon suffers a decline in NOMC after the incorporation of vanadia, in good agreement with the above XRD characterization results.

3.2 Chemical Compositions

The chemical compositions of NOMC and V$_x$O$_y$/NOMC were analyzed by XP spectroscopy (Fig. 6). Three peaks
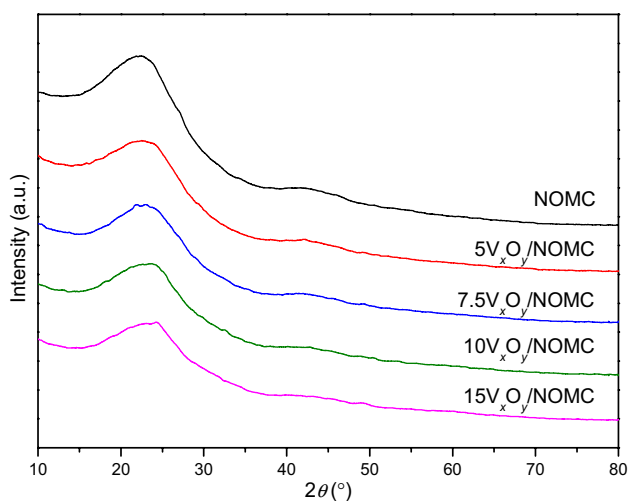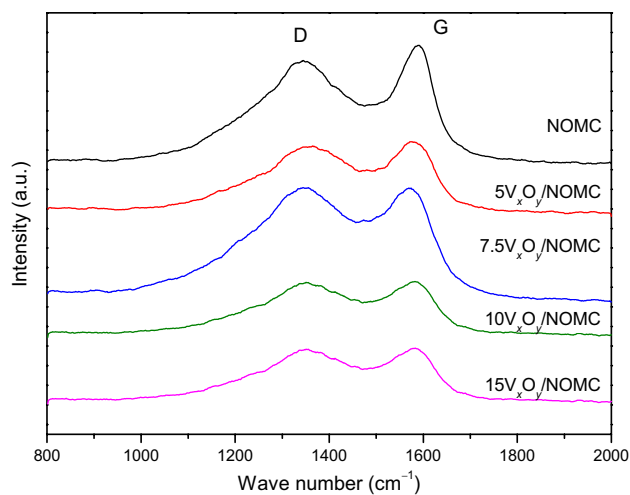
Fig. 5 Raman spectra of NOMC and V$_x$O$_y$/NOMC materials

with the binding energies of 286, 398, and 532 eV, are observed in the survey spectrum of NOMC, corresponding to carbon, nitrogen, and oxygen elements, respectively. Besides these peaks, signals located at 518 eV, associated with vanadium element, have been also detected in the spectra of V$_x$O$_y$/NOMC and vanadia materials, confirming that vanadia has been successfully loaded on the surface of the support.

In order to elucidate the chemical environment of vanadia species on the surface of the NOMC support, the high-resolution V 2p spectra of two V$_x$O$_y$/NOMC materials are further recorded (Fig. 7). Both the spectra exhibit two signals at 517.2 and 524.6 eV, attributed to 2p$_{3/2}$ and 2p$_{1/2}$ orbits of vanadium species [4, 54]. Compared with the spectra of vanadia, the positions of these signals are shifted to lower
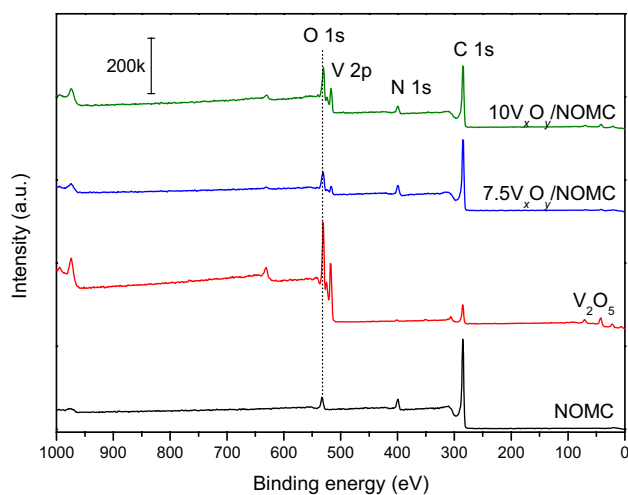
Fig. 4 Wide-angle XRD patterns of NOMC and V$_x$O$_y$/NOMC materials

Fig. 6 XPS survey of NOMC, V$_2$O$_5$, 7.5V$_x$O$_y$/NOMC, and 10V$_x$O$_y$/NOMC

Fig. 7 V 2p spectra of V_2O_5, $7.5V_xO_y$/NOMC, and $10V_xO_y$/NOMC

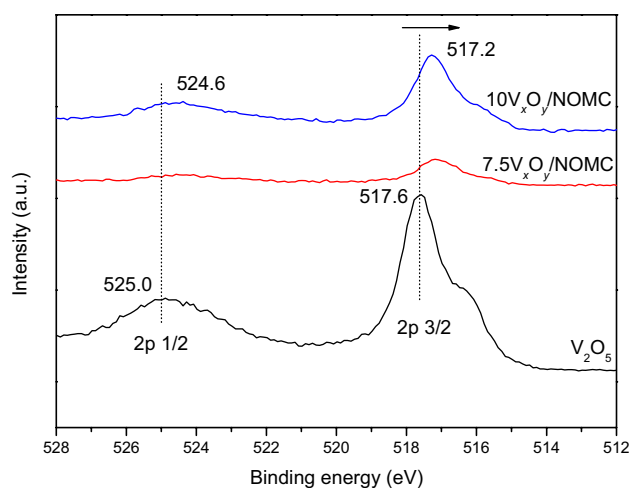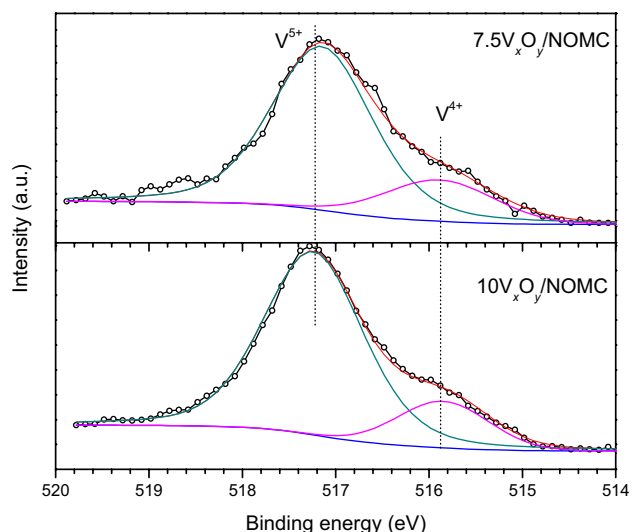**Fig. 9** N 1s spectra of NOMC, $7.5V_xO_y$/NOMC, and $10V_xO_y$/NOMC

Fig. 8 Deconvoluted V 2p spectra of $7.5V_xO_y$/NOMC and $10V_xO_y$/NOMC

Table 2 Distributions of various nitrogen species in NOMC and V_xO_y/NOMC

Material	Molar percentage (%)			
	Pyridinic	Pyrrolic	Graphitic	Pyridinic oxide
NOMC	48.8	19.4	24.0	7.8
$7.5V_xO_y$/NOMC	42.4	27.1	19.2	11.3
$10V_xO_y$/NOMC-M	44.9	29.5	18.7	6.9

binding energies in the cases of V_xO_y/NOMC. The comparison implies that vanadia species are chemically bonded on the surface of NOMC, probably because of the interaction between V and N atoms of NOMC. Such a phenomenon has been also found in carbon-nitride-supporting vanadia materials [55–57]. The deconvoluted V $2p_{3/2}$ spectra are depicted in Fig. 8. The vanadia species of V_xO_y/NOMC can be divided into V^{5+} (517.8 eV) and V^{4+} (515.9 eV) species. In general, for most oxidative reactions catalyzed by metal oxides, the existence of two variable valences is necessary for the catalytic cycle based on the Mars-van Krevelen mechanism. According to the deconvolution, the percentages of V^{4+} in $7.5V_xO_y$/NOMC and $10 V_xO_y$/NOMC are ca. 19.1% and 16.8%, higher than the value obtained in the pure vanadia (14.2%).
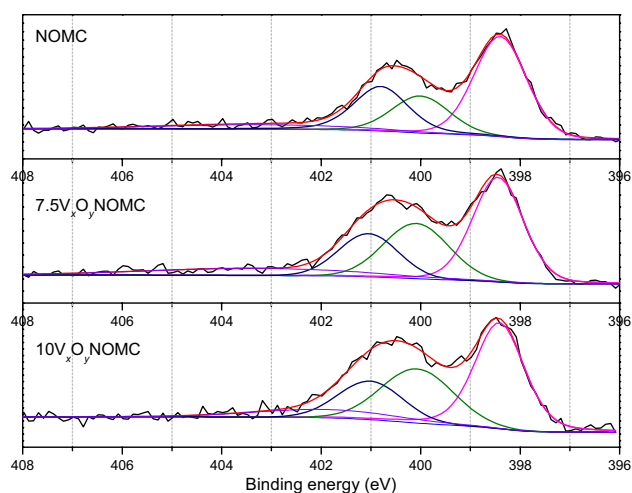
As well as V 2p, N 1s spectra (Fig. 9) of NOMC and V_xO_y/NOMC have been also collected. According to the previous papers involving the synthesis and characterization of NOMC materials [44, 48], the spectra could be deconvoluted into four independent peaks. The major peaks with the lowest binding energy of 398.4 eV correspond to the pyridinic nitrogen. The peaks located at 400.1 and 400.8 eV are assigned to pyrrolic and graphitic (also called as tertiary amine) nitrogen. The broad signals with the highest binding energy (403.2 eV) are associated with pyridinic oxides. The detailed distributions of various nitrogen species based on the deconvoluted spectra have been calculated and summarized in Table 2. The percentage of graphitic nitrogen shows a remarkable decrease in NOMC after the loading of vanadium oxide, suggesting that the graphitic nitrogen species might act as anchoring sites for vanadium oxide on the surface of NOMC. Combining the above results from V 2p and N 1 s spectra, we surmise that there might be d-p interaction between vanadia and nitrogen of NOMC, which has been also founded in the metal-doped carbon nitride materials [58, 59].

3.3 Catalyst Evaluation

The catalytic performances of the synthesized materials were evaluated in the selective oxidative of BZA using oxygen as an oxidant (Table 3). Initially, in the case of the blank experiment without any catalysts, BZA is rarely converted. Using NOMC or pure vanadia as a catalyst, the conversion of BZA is less than 15%. The use of V_xO_y/NOMC catalysts offers a remarkable improvement in the catalytic reaction and the selectivities obtained are all above 99%. Meanwhile, the target molecule, i.e. benzaldehyde, contributes more than 99% of the products, and the by-product is benzoic acid that comes from deep oxidation of benzaldehyde. Moreover, as the loading amount of vanadia is increased from 5 to 10%, the conversion of BZA is increased progressively. However, higher loading amounts of vanadia of V_xO_y/NOMC result in a decline of catalytic activity, probably due to the lower surface areas of these catalysts than $10V_xO_y$/NOMC (Table 1). It is worth noting that, in the presence of some transition-metal compounds [60], toluene could be catalytically oxidized into benzaldehyde. Regarding this, a control experiment without BZA was performed using $10V_xO_y$/NOMC as a catalyst. The corresponding catalytic conversion of toluene and selectivity to benzaldehyde were < 1% and 99%, respectively, indicating that the oxidation of toluene could rarely occur in the presence of $10V_xO_y$/NOMC catalyst. On the other hand, the control experiment suggests that in this study, the formed benzaldehyde was generated by the oxidation of BZA.

Table 3 Catalytic performances of various catalysts in the selective oxidation of BZA[a]

Catalyst	Con. (%)	Sel. (%)
–	< 1	99
NOMC	13	99
V_2O_5	8	94
$5V_xO_y$/NOMC	35	99
$7.5V_xO_y$/NOMC	43	99
$10V_xO_y$/NOMC	57	99
$12.5V_xO_y$/NOMC	51	99
$15V_xO_y$/NOMC	46	99
$10V_xO_y$/NOMC-350	52	99
$10V_xO_y$/NOMC-450	50	99
$10V_xO_y$/NOMC-500	45	99
$10V_xO_y$/SBA-15	21	99
$10V_xO_y$/mpg-C_3N_4	43	99
$10V_xO_y$/NOMC [b]	< 1	99

[a]Reaction conditions: $n_{BZA} = 1$ mmol, $V_{toluene} = 5$ mL, $W = 0.1$ g, $T = 95$ °C, $t = 8$ h

[b]Without BZA

Besides the loading amount, the preparation temperature of V_xO_y/NOMC has an impact on the final catalytic activity. As listed in Table 3, $10V_xO_y$/NOMC-400 affords the highest catalytic conversion (57%) under the same reaction conditions. It is reasonable to surmise that the steady interaction between V and N demands a suitable preparation temperature. As well as NOMC, vanadia catalysts supported on ordered mesoporous silica SBA-15 and mesoporous carbon graphite (mpg-C_3N_4) materials were also synthesized. As listed in Table 3, the two supported vanadia catalysts show inferior activities to $10V_xO_y$/NOMC. Although SBA-15 owns a much larger surface area (> 560 m^2 g^{-1}) than NOMC, the mesoporous silica has no nitrogen-containing species as effective anchoring sites for vanadia species. The lower activity of $10V_xO_y$/mpg-C_3N_4 might be due to the difference in terms of nitrogen distributions between mpg-C_3N_4 (heptazine) and NOMC (pyridinic/pyrrolic/graphitic nitrogen).

The influences of reaction conditions on the catalytic performances are subsequently investigated using $10V_xO_y$/NOMC as a catalyst (Fig. 10). The conversion of BZA acquired at the first 2 h of reaction time is only 12%; prolonging the reaction, the conversion is elevated progressively. As the reaction proceeds for 12 h, the conversion can be up to 80%. Likewise, the catalytic conversion is also sensitive to the reaction temperature. Adopting higher temperatures leads to a continuous improvement in the conversion of BZA, while the selectivities gained from 75 to 115 °C are still above 99%. The relation between conversion of BZA and the catalyst weight is plotted as Fig. 10C. As the catalyst weight is added, the conversion is increased continuously. Notwithstanding, upon adopting a higher amount of catalyst, the conversion seems to increase slightly.

To test the adsorptive capability of the $10V_xO_y$/NOMC catalyst of BZA and benzaldehyde in the catalytic reaction, a series of liquid-phase adsorption experiments were conducted and the resultant adsorption-equilibrium data were given in Fig. 11. Either in the BZA−toluene or benzaldehyde−toluene solution, the equilibrium concentrations of BZA or benzaldehyde are all below the corresponding initial concentrations. Moreover, under the same initial concentration of BZA and benzaldehyde, the equilibrium concentration of BZA is lower than that of benzaldehyde, verifying that the adsorptive capability of BZA over the catalyst is higher than that of benzaldehyde. The difference in adsorptive capability about the two compounds is beneficial to adsorption and then activation of BZA and simultaneous desorption of benzaldehyde on the surface of the catalyst.

Recyclability is also an important parameter to examine a heterogeneous catalyst. Fig. 12 shows the catalytic performances of $10V_xO_y$/NOMC catalyst within the five consecutive experiments. After each catalytic run, the catalyst was filtrated, rinsed by ethanol, and dried. Within
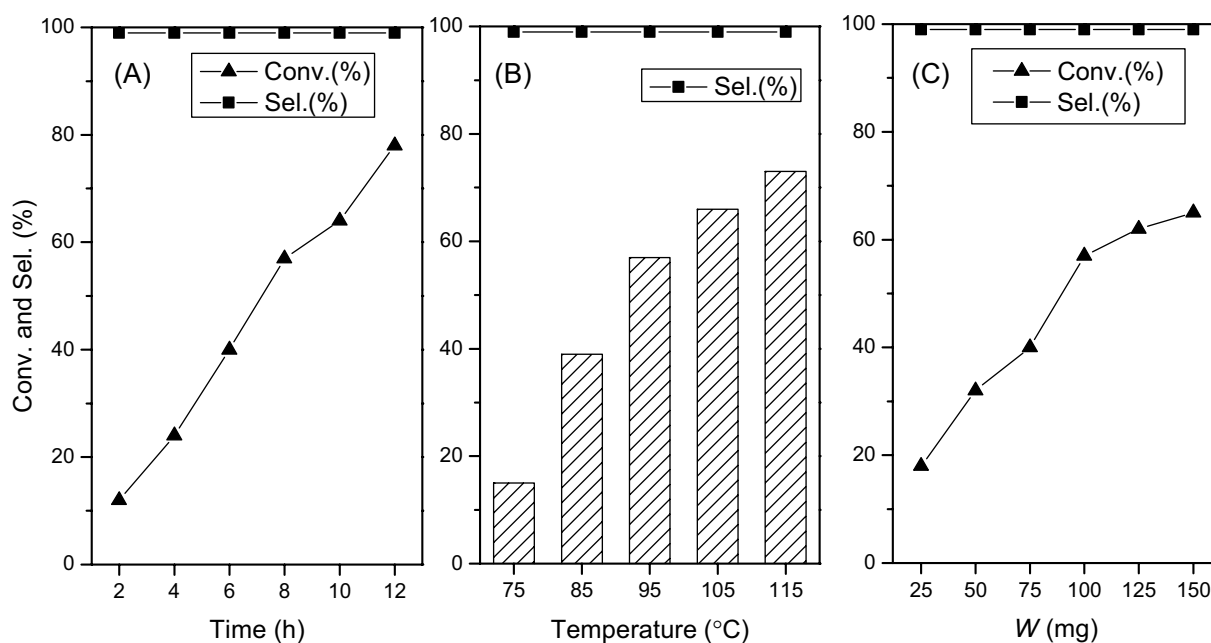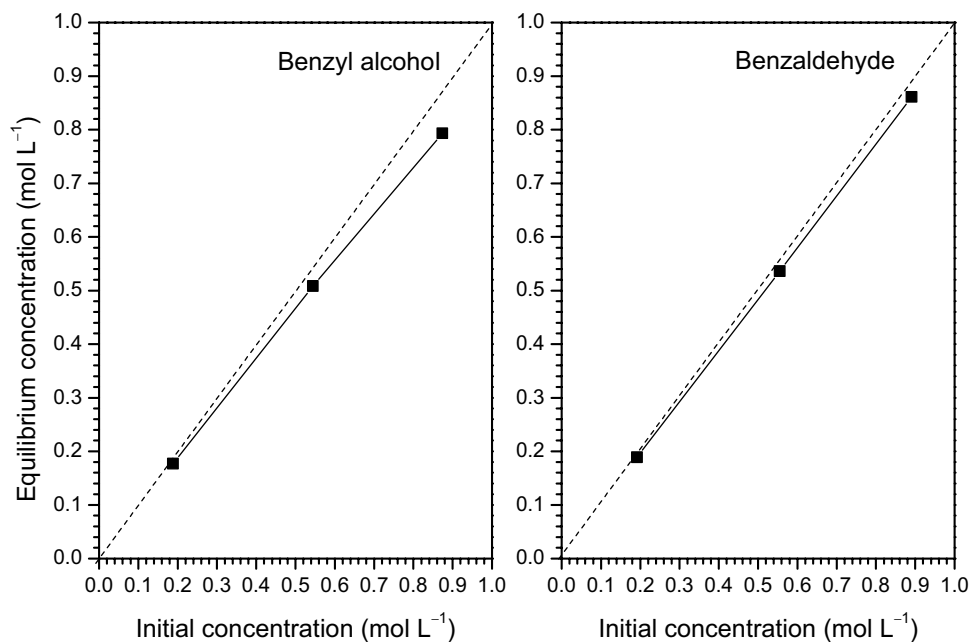
Fig. 10 Effects of reaction time (**A**), temperature (**B**), and catalyst weight (**C**) on the catalytic performance $10V_xO_y$/NOMC. Reaction conditions: $n_{BZA} = 1$ mmol, $V_{toluene} = 5$ mL, $W = 0.1$ g (**A**, **B**), $T = 95$ °C (**A**, **C**), and $t = 8$ h (**B**, **C**)

Fig. 11 Initial and equilibrium concentrations of BZA and benzaldehyde over $10V_xO_y$/NOMC under various concentrations

the five runs, the selectivities are all above 99%. As for the catalytic conversion, the value is decreased from 57% to 32%. It should be noted that the decline is attributed to the loss of catalyst during the recycling experiment. In fact, if taking into account the weight of the recycled catalyst, the specific activity of $10V_xO_y$/NOMC is relatively stable.

4 Conclusion

In summary, V_xO_y/NOMC catalysts were prepared by utilizing nitrogen-containing ordered mesoporous carbon materials (NOMCs) as catalytic supports. Vanadium oxide nanoparticles were well dispersed in the mesoporous
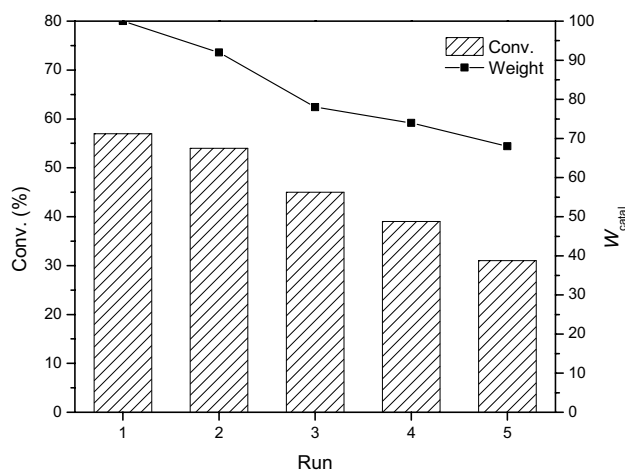
Fig. 12 Catalytic performances of $10V_xO_y$/NOMC during five consecutive runs

channels of NOMC supports. The characterization results indicated that the loading of vanadia has not altered the overall ordered mesostructures of NOMC, and there was a stable interaction between V and N of NOMC. In the selective oxidation of benzyl alcohol using oxygen as an oxidant, the synthesized V_xO_y/NOMC materials showed good and stable catalytic performance. Moreover, the activity of V_xO_y/NOMC was superior to the vanadia catalysts supported on SBA-15 and mesoporous carbon nitride materials under the same reaction conditions.

Declarations

Conflict of interest There are no conflicts of interest to declare for each contributing author.

References

1. Zhang K, Liu Y, Deng J, Jing L, Pei W, Han Z, Zhang X, Dai H (2019) ChemCatChem 11:6398–6407
2. Li Y, Sabbaghi A, Huang J, Li KC, Tsui LS, Lam FL, Hu X (2020) Mol Catal 485:110789
3. Arena F, Gumina B, Lombardo AF, Espro C, Patti A, Spadaro L, Spiccia L (2015) Appl Catal B 162:260–267
4. Huang G, Xiang F, Li T, Jiang Y, Guo Y (2011) Catal Commun 12:886–889
5. Huang Z, Yan F, Yuan G (2017) Catal Lett 147:509–516
6. Hao Y, Hao G-P, Guo D-C, Guo C-Z, Li W-C, Li M-R, Lu A-H (2012) ChemCatChem 4:1595–1602
7. Della Pina C, Falletta E, Rossi M (2008) J Catal 260:384–386
8. Wang X, Wu G, Guan N, Li L (2012) Appl Catal B 115–116:7–15
9. Che J, Hao M, Yi W, Kobayashi H, Zhou Y, Xiao L, Fan J (2017) Chin J Catal 38:1870–1879
10. Xiao S, Zhang C, Chen R, Chen F (2015) New J Chem 39:4924–4932
11. Guo Z, Liu B, Zhang Q, Deng W, Wang Y, Yang Y (2014) Chem Soc Rev 43:3480–3524
12. Choudhary VR, Dhar A, Jana P, Jha R, Uphade BS (2005) Green Chem 7:768–770
13. Xu J, Shang J-K, Wang Y, Chen Y, Li Y-X (2017) Catal Lett 147:328–334
14. Alhumaimess M, Lin Z, Weng W, Dimitratos N, Dummer NF, Taylor SH, Bartley JK, Kiely CJ, Hutchings GJ (2012) Chemsuschem 5:125–131
15. Yang J, Cao K, Gong M, Shan B, Chen R (2020) J Catal 386:60–69
16. Xu J, Shang J-K, Chen Y, Wang Y, Li Y-X (2017) Appl Catal A 542:380–388
17. Besson M, Gallezot P (2000) Catal Today 57:127–141
18. Davis SE, Ide MS, Davis RJ (2013) Green Chem 15:17–45
19. Su F-Z, Liu Y-M, Wang L-C, Cao Y, He H-Y, Fan K-N (2008) Angew Chem Int Ed 47:334–337
20. Abad A, Concepción P, Corma A, García H (2005) Angew Chem Int Ed 44:4066–4069
21. Moreno I, Dummer NF, Edwards JK, Alhumaimess M, Sankar M, Sanz R, Pizarro P, Serrano DP, Hutchings GJ (2013) Catal Sci Technol 3:2425–2434
22. Wang Q, Cai X, Liu Y, Xie J, Zhou Y, Wang J (2016) Appl Catal B 189:242–251
23. Song H, Liu Z, Gai H, Wang Y, Qiao L, Zhong C, Yin X, Xiao M (2019) Front Chem 7:458
24. Hong H, Hu L, Li M, Zheng J, Sun X, Lu X, Cao X, Lu J, Gu H (2011) Chem Eur J 17:8726–8730
25. Sun Y, Li X, Wang J, Ning W, Fu J, Lu X, Hou Z (2017) Appl Catal B 218:538–544
26. Liu J, Yuan Q, Zhao H, Zou S (2018) Catal Lett 148:1093–1099
27. Göksu H, Burhan H, Mustafov SD, Şen F (2020) Sci Rep 10:5439
28. Zhu J, Faria JL, Figueiredo JL, Thomas A (2011) Chem Eur J 17:7112–7117
29. Zhu Y, Dong Y, Zhao L, Yuan F (2010) J Mol Catal A 315:205–212
30. Velusamy S, Punniyamurthy T (2004) Org Lett 6:217–219
31. Feng T, Vohs JM (2005) J Phys Chem B 109:2120–2127
32. Srilakshmi C, Basava V, Ramesh G, Manjunath M (2020) ChemistrySelect 5:4500–4508
33. Kara GK, Rahimi J, Niksefat M, Taheri-Ledari R, Rabbani M, Maleki A (2020) Mater Chem Phys 250:122991
34. Renuka MK, Gayathri V (2019) Catal Lett 149:1266–1276
35. Xu J, Liu Y-M, Xue B, Li Y-X, Cao Y, Fan K-N (2011) Phys Chem Chem Phys 13:10111–10118
36. Grzybowska-Świerkosz B (1997) Appl Catal A 157:263–310
37. Li M, Xu F, Li H, Wang Y (2016) Catal Sci Technol 6:3670–3693
38. Shen W, Fan W (2013) J Mater Chem A 1:999–1013
39. Xie M, Xia Y, Liang J, Chen L, Guo X (2014) Micropor Mesopor Mater 197:237–243
40. Chen P, Yang C, He Z, Guo K (2019) J Mater Sci 54:4180–4191
41. Liu L, Xu S-D, Wang F-Y, Song Y-J, Liu J, Gao Z-M, Yuan Z-Y (2017) RSC Adv 7:12524–12533

42. Yu J, Guo M, Muhammad F, Wang A, Zhang F, Li Q, Zhu G (2014) Carbon 69:502–514
43. Zhou S, Xu H, Yuan Q, Shen H, Zhu X, Liu Y, Gan W (2015) ACS Appl Mater Inter 8:918–926
44. Wang J, Liu H, Gu X, Wang H, Su DS (2014) Chem Commun 50:9182–9184
45. Qin L, Wang L, Wang C, Yang X, Lv B (2019) Mol Catal 462:61–68
46. Xue B, Wen L-Z, Ma D, Li M-M, Xu J (2018) Res Chem Intermed 44:7641–7655
47. Zhang L, Wang H, Qin Z, Wang J, Fan W (2015) RSC Adv 5:22838–22846
48. Wang J, Liu H, Diao J, Gu X, Wang H, Rong J, Zong B, Su DS (2015) J Mater Chem A 3:2305–2313
49. Watanabe H, Asano S, Fujita S, Yoshida H, Arai M (2015) ACS Catal 5:2886–2894
50. Datta KKR, Reddy BVS, Ariga K, Vinu A (2010) Angew Chem Int Ed 49:5961–5965
51. Hu L, Wang C, Yue B, Chen X, He H (2016) RSC Adv 6:87656–87664
52. Liu D, Lei J-H, Guo L-P, Qu D, Li Y, Su B-L (2012) Carbon 50:476–487
53. Mane GP, Talapaneni SN, Anand C, Varghese S, Iwai H, Ji Q, Ariga K, Mori T, Vinu A (2012) Adv Funct Mater 22:3596–3604
54. Borah P, Ma X, Nguyen KT, Zhao Y (2012) Angew Chem Int Ed 51:7756–7761
55. Xu J, Chen Y, Hong Y, Zheng H, Ma D, Xue B, Li Y-X (2018) Appl Catal A 549:31–39
56. Xu J, Jiang Q, Chen T, Wu F, Li Y-X (2015) Catal Sci Technol 5:1504–1513
57. Verma S, Baig RBN, Nadagouda MN, Varma RS (2016) ACS Sustain Chem Eng 4:1094–1098
58. Wang X, Chen X, Thomas A, Fu X, Antonietti M (2009) Adv Mater 21:1609–1612
59. Xu J, Long K-Z, Wang Y, Xue B, Li Y-X (2015) Appl Catal A 496:1–8
60. Valentini F, Ferracci G, Galloni P, Pomarico G, Conte V, Sabuzi F (2021) Catalysts 11:262

Authors and Affiliations

Xin-Tong Yi[1] · **Tian-Lu Wang**[1] · **Lin-Zhi Wen**[1] · **Jie Xu**[1] · **Bing Xue**[1]

1   Jiangsu Key Laboratory of Advanced Catalytic Materials and Technology, School of Petrochemical Engineering, Changzhou University, Gehu Middle Road 21, Changzhou, Jiangsu 213164, People's Republic of China